

# Photon emission from inside the innermost stable circular orbit

Takahisa Igata,<sup>1,\*</sup> Kazunori Kohri,<sup>1,2,3,†</sup> and Kota Ogasawara<sup>4,‡</sup>

<sup>1</sup>*KEK Theory Center, Institute of Particle and Nuclear Studies,  
High Energy Accelerator Research Organization, Tsukuba 305-0801, Japan*

<sup>2</sup>*The Graduate University of Advanced Studies (SOKENDAI), Tsukuba 305-0801, Japan*

<sup>3</sup>*Kavli Institute for the Physics and Mathematics of the Universe (WPI),  
University of Tokyo, Kashiwa 277-8583, Japan*

<sup>4</sup>*Theoretical Astrophysics Group, Department of Physics,  
Kyoto University, Kyoto 606-8502, Japan*

(Dated: January 5, 2022)

We consider a situation where a light source orbiting the innermost stable circular orbit (ISCO) of the Kerr black hole is gently falling from the marginally stable orbit due to an infinitesimal perturbation. Assuming that the light source emits photons isotropically, we show that the last radius at which more than 50% of emitted photons can escape to infinity is approximately halfway between the ISCO radius and the event horizon radius. To evaluate them, we determine emitter orbits from the vicinity of the ISCO, which are uniquely specified for each black hole spin, and identify the conditions for a photon to escape from any point on the equatorial plane of the Kerr spacetime to infinity by specifying regions in the two-dimensional photon impact parameter space completely. We further show that the proper motion of the emitter affects the photon escape probability and blueshifts the energy of emitted photons.

## I. INTRODUCTION

In recent years, significant progress has been made in observing a massive compact object located at the center of a galaxy. The shadow observation of the M87 galactic center suggests that the central object is a black hole [1]. In principle, we cannot receive any signals coming from inside the black hole because nothing can escape from it, but we can observe phenomena just outside the event horizon. In other words, all the observations of black holes, including the shadow observations, without exception focus on unique phenomena in the vicinity of the horizon. However, naively, the strong gravitational sphere of a black hole does not allow most signals emitted

---

\* [igata@post.kek.jp](mailto:igata@post.kek.jp)

† [kohri@post.kek.jp](mailto:kohri@post.kek.jp)

‡ [kota@tap.scphys.kyoto-u.ac.jp](mailto:kota@tap.scphys.kyoto-u.ac.jp)

from the region close to the horizon to escape. Therefore, some mechanisms to increase the escape probability of such signals are necessary to observe unique phenomena near the horizon [2].

Recently, the escape probability of photons emitted isotropically from an emitter orbiting a circular geodesic near a Kerr black hole was shown to be more than 50% for an arbitrary black hole spin parameter and an arbitrary orbital radius [3, 4]. Furthermore, depending on the direction of the emission, the Doppler shift cancels the gravitational redshift, and as a result, the signals can reach a distant observer in observable bands [3, 5, 6]. The mechanism common to both phenomena is a relativistic boost or beaming due to the proper motion of the emitter. In recent years, such the relativistic effects have been actively investigated through observations of a star orbiting around the center of our galaxy [7–9]. Even though the radius of the innermost stable circular orbit (ISCO) arbitrarily approaches the horizon radius in the maximum spin limit, the escape probability still exceeds a half [3, 4], and the Doppler blueshift is still dominant at least for the forward emission, suggesting that the emitter on the ISCO is a useful probe of the near-horizon. In fact, a light source that seems to be orbiting the ISCO was observed [10]. In particular, in the Atacama Large Millimeter/submillimeter Array observations of Sagittarius A\*—a black hole candidate with an accretion disk at the center of our galaxy—a short-timescale variation of the radio flux density was reported [11]. This variation timescale ( $\sim 30$  minutes) is comparable to the orbital period of the Schwarzschild ISCO ( $\sim 3r_g$ , where  $r_g$  is the Schwarzschild radius). We can interpret this phenomenon as a sign that a hot spot is orbiting on the inner edge of the accretion disk and as the appearance of the relativistic beaming effect due to orbiting at high speed.

If an object orbiting the ISCO, such as a hot spot, is perturbed slightly, it must transit from the marginal orbit to a plunge orbit into the center. If we continue to receive signals from the falling emitter, to what depth of the gravitational potential will we achieve the observation? In other words, if we assume that the escape probability of a photon is 50% or more as an indicator of observability, what is the last radius where the probability becomes a half? This threshold value is closely related to the unstable photon circular orbit [12] and appears in the context of the loosely trapped surfaces [13], which are the recent development of photon surfaces [14–16]. The purpose of this paper is to identify some thresholds related to the photon escape probability if the emitter *gently* leaves the ISCO and falls into the black hole.

This paper is organized as follows. In Sec. II, we review a formulation of particle motion in the Kerr spacetime. In Sec. III, clarifying necessary and sufficient escape conditions for photons emitted from the equatorial plane, we completely specify the photon escape parameter region in the space of impact parameters. In Sec. IV, we describe the dynamics of an emitter plunging from

the ISCO into the horizon. In Sec. V, formulating the escape probability of a photon measured in the rest frame of the emitter, we evaluate the photon escape probability for each black hole spin and discuss some properties relevant to the emitter dynamics. Section VI is devoted to a summary and discussions. In this paper, we use units in which  $G = 1$  and  $c = 1$ .

## II. GEODESIC SYSTEM IN THE KERR SPACETIME

The Kerr spacetime metric in the Boyer-Lindquist coordinates is given by

$$g_{\mu\nu}dx^\mu dx^\nu = -\frac{\Delta\Sigma}{A}dt^2 + \frac{\Sigma}{\Delta}dr^2 + \Sigma d\theta^2 + \frac{A}{\Sigma}\sin^2\theta\left(d\varphi - \frac{2Mar}{A}dt\right)^2, \quad (1)$$

$$\Delta = r^2 - 2Mr + a^2, \quad \Sigma = r^2 + a^2\cos^2\theta, \quad A = (r^2 + a^2)^2 - a^2\Delta\sin^2\theta, \quad (2)$$

where  $M$  and  $a$  are mass and spin parameters, respectively. We assume that the metric denotes a black hole spacetime, i.e.,  $0 \leq a \leq M$ . Then, the event horizon is located at  $r = r_H := M + \sqrt{M^2 - a^2}$ . The metric admits a stationary Killing vector  $\partial/\partial t$ , an axial Killing vector  $\partial/\partial\varphi$ , and a nontrivial rank-2 Killing tensor [17]

$$K_{ab} = \Sigma^2(d\theta)_a(d\theta)_b + \sin^2\theta[(r^2 + a^2)(d\varphi)_a - a(dt)_a][(r^2 + a^2)(d\varphi)_b - a(dt)_b] - a^2\cos^2\theta g_{ab}. \quad (3)$$

We consider a freely falling particle system (i.e., a geodesic system) in the Kerr spacetime. Let  $p_a$  be a canonical momentum of a particle, and let  $H$  be the Hamiltonian of affinely parametrized geodesic system,

$$H = \frac{1}{2}g^{ab}p_ap_b = \frac{1}{2}\left[\frac{\Delta}{\Sigma}p_r^2 + \frac{p_\theta^2}{\Sigma} + \frac{\Sigma}{A\sin^2\theta}p_\varphi^2 - \frac{A}{\Delta\Sigma}\left(p_t + \frac{2Mar}{A}p_\varphi\right)^2\right], \quad (4)$$

where  $g^{ab}$  is the inverse metric. Since  $t$  and  $\varphi$  are cyclic variables in  $H$ , the conjugate momentum components  $p_t = -E$  and  $p_\varphi = L$  are constants of motion. We can interpret  $E$  and  $L$  as conserved energy and angular momentum along a geodesic, respectively. From reparameterization invariance of an affine parameter, a particle must satisfy the constraint condition

$$\kappa = -g^{ab}p_ap_b, \quad (5)$$

where  $\kappa = 1$  for a massive particle with unit mass, and  $\kappa = 0$  for a massless particle. From the existence of the Killing tensor (3), a particle has another quadratic constant of motion in  $p_a$ , the so-called Carter constant,

$$Q = K^{ab}p_ap_b - (L - aE)^2. \quad (6)$$

The four constants of motion commute with each other in the Poisson brackets. Therefore, the equation of motion (i.e., the geodesic equation) in the Kerr spacetime is integrable in the Liouville sense.

Not only is it integrable, but it causes the separation of variables in the Boyer-Lindquist coordinates by using the Hamilton-Jacobi method [18]. The separated equations in the canonical variables are rewritten by the derivatives  $\dot{x}^\mu$  with respect to the affine parameter as

$$\Sigma \dot{t} = a(L - aE \sin^2 \theta) + \frac{r^2 + a^2}{\Delta} [(r^2 + a^2)E - aL], \quad (7)$$

$$\Sigma \dot{\phi} = \frac{L - aE \sin^2 \theta}{\sin^2 \theta} + \frac{a}{\Delta} [(r^2 + a^2)E - aL], \quad (8)$$

$$\Sigma \dot{r} = \sigma_r \sqrt{R_\kappa}, \quad (9)$$

$$\Sigma \dot{\theta} = \sigma_\theta \sqrt{\Theta_\kappa}, \quad (10)$$

where  $\sigma_r = \text{sgn}(\dot{r})$ ,  $\sigma_\theta = \text{sgn}(\dot{\theta})$ , and

$$R_\kappa(r) = [(r^2 + a^2)E - aL]^2 - \Delta [(L - aE)^2 + Q + \kappa r^2], \quad (11)$$

$$\Theta_\kappa(\theta) = Q - \cos^2 \theta \left[ \frac{L^2}{\sin^2 \theta} + a^2(\kappa - E^2) \right]. \quad (12)$$

Note that  $R_\kappa$  and  $\Theta_\kappa$  must be nonnegative for physical solutions, as is seen from Eqs. (9) and (10). We use units in which  $M = 1$  in what follows.

### III. PHOTON ESCAPE CONDITIONS

We consider escape conditions of a photon (i.e.,  $\kappa = 0$ ) emitted from a point on the equatorial plane. Let us denote a momentum of a photon as  $k_a$  instead of  $p_a$ . Since only considering a photon escaping to infinity, without loss of generality, we may assume that  $E > 0$ . It is useful to introduce impact parameters

$$b = \frac{L}{E}, \quad q = \frac{Q}{E^2}. \quad (13)$$

Rescaling  $k^a$  as  $k^a/E \rightarrow k^a$ , we obtain a two-parameter family of the null geodesic equations parametrized by  $(b, q)$ .

Let  $\theta_*$  be the polar angle coordinate value of the emission point, i.e.,  $\theta_* = \pi/2$ . The function  $\Theta_0$  in Eq. (12) evaluated there leads to

$$\Theta_0(\theta_*) = q - \cot^2 \theta_* (b^2 - a^2 \sin^2 \theta_*) = q \geq 0. \quad (14)$$

Hence, a photon emitted from the equatorial plane must always have a nonnegative value of  $q$ . Hereafter, we assume that  $q \geq 0$ .

Let us clarify the escape conditions of a photon, which are determined from the radial equation of motion (9). The function  $R_0$  is factored as

$$R_0 = [r^2 + a(a - b)]^2 - \Delta [q + (b - a)^2] \quad (15)$$

$$= r(2 - r)(b - b_1)(b - b_2), \quad (16)$$

where

$$b_1(r; q) = \frac{-2ar + \sqrt{r\Delta [r^3 - q(r - 2)]}}{r(r - 2)}, \quad (17)$$

$$b_2(r; q) = \frac{-2ar - \sqrt{r\Delta [r^3 - q(r - 2)]}}{r(r - 2)}, \quad (18)$$

which show the values of  $b$  at a radial turning point. Note that  $b_2$  is singular at  $r = 2$ , but  $R_0$  is finite there. Since  $R_0 \geq 0$  must hold, the allowed range of  $b$  is restricted as

$$b_2 \leq b \leq b_1 \text{ for } r > 2, \quad (19)$$

$$b \geq b_2, \ b \leq b_1 \text{ for } r_H < r < 2. \quad (20)$$

We focus on extremum points of  $b_1$  and  $b_2$ , which characterize the photon escape conditions. The photon orbits staying at the extrema are known as the spherical photon orbits [19]. Solving equivalent conditions for the extrema,  $R_0 = 0$  and  $dR_0/dr = 0$ , we obtain  $b$  and  $q$  as functions of the spherical photon orbit radius, respectively,

$$b_{\text{SPO}}(r) = -\frac{r^3 - 3r^2 + a^2r + a^2}{a(r - 1)}, \quad (21)$$

$$q_{\text{SPO}}(r) = -\frac{r^3(r^3 - 6r^2 + 9r - 4a^2)}{a^2(r - 1)^2}. \quad (22)$$

Eliminating  $r$  from these expressions, we find the extremum values

$$b_i^s(q) = b_{\text{SPO}}(r_i(q)) \quad (i = 1, 2), \quad (23)$$

where  $r = r_i(q)$  ( $r_2 \geq r_1$ ) is the real solutions to the equation  $q = q_{\text{SPO}}$ . If  $q = 0$ , the radii  $r_i$  reduce to those of the unstable photon circular orbits

$$r_1^c = r_1(0) = 2 + 2 \cos \left[ \frac{2}{3} \arccos(a) - \frac{2\pi}{3} \right], \quad (24)$$

$$r_2^c = r_2(0) = 2 + 2 \cos \left[ \frac{2}{3} \arccos(a) \right], \quad (25)$$

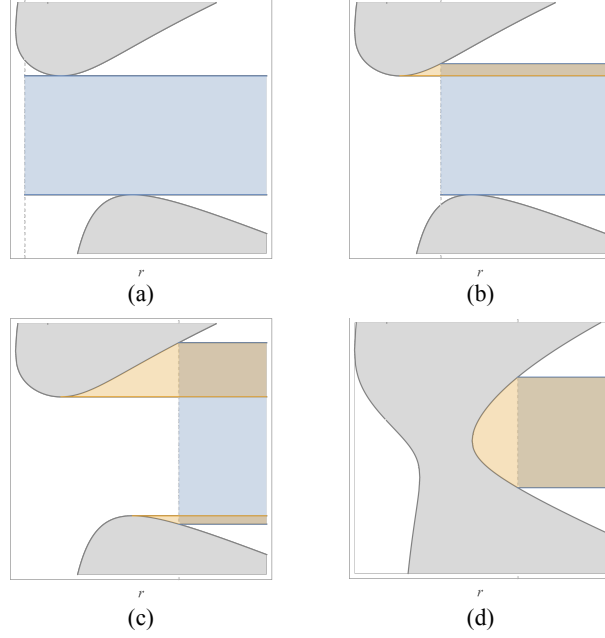


FIG. 1. Typical shape of allowed region for the radial photon motion and the parameter range of  $b$  for escape photons. Gray curves denote  $b_i$  ( $i = 1, 2$ ) as a function of  $r$  for fixed  $q$ , and gray shaded regions denote forbidden regions, while other regions denote allowed regions. Vertical dashed lines are the radial coordinate value of the emission point  $r = r_*$ . The functions  $b_i$  in (a)–(c) have extrema  $b_i^s$  at  $r = r_i$ , respectively, and are typical shape for  $0 \leq q < 27$ , where (a)  $r_H < r_* < r_1$ , (b)  $r_1 \leq r_* < r_2$ , and (c)  $r_* \geq r_2$ . The functions  $b_i$  in (d) are typical shape for  $q > 27$ , in which the allowed region is divided into two disconnected ones, and no longer have extrema. Blue and orange shaded regions show the parameter range of  $b$  for an escape photon initially with  $\sigma_r = 1$  and  $\sigma_r = -1$ , respectively.

respectively. The extremum points appear as a pair of  $r_i$  only in the range  $r_1^c \leq r_1 \leq r_2 \leq r_2^c$ , and the corresponding range of  $q$  is  $0 \leq q \leq 27$ . The pair coincides with each other at  $r_1 = r_2 = 3$ , where  $q = 27$ .

We can see typical shape of  $b_i$  as gray curves in Figs. 1(a)–1(c) for  $0 \leq q < 27$  and in Fig. 1(d) for  $q > 27$ . Gray shaded regions denote forbidden regions of photon motion, while other regions denote allowed regions. Let us use them to specify whole parameter regions of photon escape in a visual manner. Let  $r_*$  be the radial coordinate value of the emission point, which is drawn by dashed vertical lines in the figures. In the case  $r_H < r_* < r_1$ , only photons initially emitted outward (i.e.,  $\sigma_r = 1$ ) with  $b_2^s < b < b_1^s$  can escape [see blue shaded region in Fig. 1(a)]. In the case  $r_1 \leq r_* < r_2$ , photons initially emitted outward (i.e.,  $\sigma_r = 1$ ) with  $b_2^s < b \leq b_1(r_*; q)$  can escape [see blue shaded region in Fig. 1(b)], and photons initially emitted inward (i.e.,  $\sigma_r = -1$ ) with  $b_1^s < b < b_1(r_*; q)$  also can escape [see orange shaded region in Fig. 1(b)]. In the case  $r_* \geq r_2$ , photons initially emitted

TABLE I. Photon escape parameter region in the Kerr spacetime.

Case	$q$	$b$ ( $\sigma_r = +$ )	$b$ ( $\sigma_r = -$ )
(i) $r_H < r_* < r_1^c$	$0 \leq q \leq 27$	$b_2^s < b < b_1^s$	n/a
(ii) $r_1^c \leq r_* < 3$	$0 \leq q < q_*$	$b_2^s < b \leq b_1(r_*, q)$	$b_1^s < b < b_1(r_*, q)$
	$q_* \leq q \leq 27$	$b_2^s < b < b_1^s$	n/a
(iii) $3 \leq r_* < r_2^c$	$0 \leq q < q_*$	$b_2^s < b \leq b_1(r_*, q)$	$b_1^s < b < b_1(r_*, q)$
	$q_* \leq q < 27$	$b_2(r_*, q) \leq b \leq b_1(r_*, q)$	$b_2(r_*, q) < b < b_2^s, b_1^s < b < b_1(r_*, q)$
	$27 \leq q \leq q_{\max}$	$b_2(r_*, q) \leq b \leq b_1(r_*, q)$	$b_2(r_*, q) < b < b_1(r_*, q)$
(iv) $r_2^c \leq r_*$	$0 \leq q < 27$	$b_2(r_*, q) \leq b \leq b_1(r_*, q)$	$b_2(r_*, q) < b < b_2^s, b_1^s < b < b_1(r_*, q)$
	$27 \leq q \leq q_{\max}$	$b_2(r_*, q) \leq b \leq b_1(r_*, q)$	$b_2(r_*, q) < b < b_1(r_*, q)$

outward (i.e.,  $\sigma_r = 1$ ) with  $b_2(r_*, q) \leq b \leq b_1(r_*, q)$  can escape [see blue shaded region in Fig. 1(c)], and photons initially emitted inward (i.e.,  $\sigma_r = -1$ ) with  $b_1^s < b < b_1(r_*, q)$  or  $b_2(r_*, q) < b < b_2^s$  also can escape [see orange shaded region in Fig. 1(c)]. For  $q \geq 27$ , note that the allowed region is disconnected. Therefore, if  $r_*$  takes a value in the outer allowed region, then photons must have  $b_2(r_*, q) \leq b \leq b_1(r_*, q)$  and always can escape [see blue and orange shaded region in Fig. 1(d)].

Let us summarize the photon escape conditions as a region in the  $(b, q)$  parameter space for a fixed  $r_*$ . To complete it, we introduce the following four ranges of  $r_*$ :

$$(i) \ r_H < r_* < r_1^c, \quad (26)$$

$$(ii) \ r_1^c \leq r_* < 3, \quad (27)$$

$$(iii) \ 3 \leq r_* < r_2^c, \quad (28)$$

$$(iv) \ r_2^c \leq r_*. \quad (29)$$

To identify the photon escape parameter regions completely, we introduce two specific values of  $q$ ,

$$q_* = q_{\text{SPO}}(r_*), \quad (30)$$

$$q_{\max} = \frac{r_*^3}{r_* - 2}. \quad (31)$$

For  $q = r^3/(r - 2)$ , the functions  $b_{1,2}$  are degenerate, and for  $q > r^3/(r - 2)$ , the position  $r$  enters the forbidden region. Therefore, the maximum value of  $q$  is limited by  $q_{\max}$  for the photon emission. Finally, we can summarize the photon escape parameter region in the  $(b, q)$  plane as Table I. Though the photon escape regions shown in Refs. [20, 21] were only Cases (i) and (ii), here we have identified them for all the ranges of  $r_*$ .

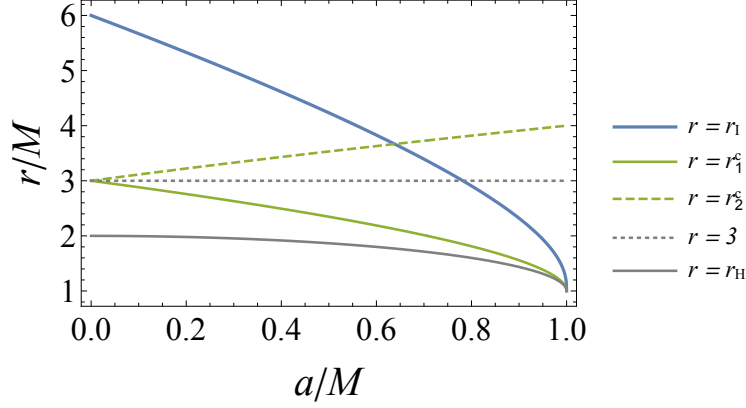


FIG. 2. Characteristic radii of particle circular orbits as functions of  $a$ . Blue solid curve: the ISCO radius given by Eq. (35). Green solid curve: the radius of photon circular prograde orbit given by Eq. (24). Green dashed curve: the radius of photon circular retrograde orbit given by Eq. (25). Gray dotted line is  $r = 3$ , and gray solid curve denotes the horizon radius. The equality  $r_I = r_1^c$  holds at  $a = 0.6382\dots$ , and  $r_I = 3$  holds at  $a = 0.7818\dots$

#### IV. DYNAMICS OF AN EMITTER

We consider an emitter ( $\kappa = 1$ ) freely falling from the ISCO into the horizon. Assume that the emitter moves on  $\theta = \pi/2$  and has the same energy and angular momentum as those of a particle orbiting the ISCO. Then, the constants  $Q$ ,  $E$ , and  $L$  of the emitter are

$$Q = 0, \quad (32)$$

$$E = \frac{r_I^{3/2} - 2r_I^{1/2} + a}{r_I^{3/4}(r_I^{3/2} - 3r_I^{1/2} + 2a)^{1/2}}, \quad (33)$$

$$L = \frac{r_I^2 - 2ar_I^{1/2} + a^2}{r_I^{3/4}(r_I^{3/2} - 3r_I^{1/2} + 2a)^{1/2}}, \quad (34)$$

where  $r_I$  is the radius of the ISCO [22],

$$r_I = 3 + Z_2 - [(3 - Z_1)(3 + Z_1 + 2Z_2)]^{1/2}, \quad (35)$$

$$Z_1 = 1 + (1 - a^2)^{1/3} \left[ (1 + a)^{1/3} + (1 - a)^{1/3} \right], \quad (36)$$

$$Z_2 = (3a^2 + Z_1^2)^{1/2}. \quad (37)$$

Figure 2 shows the relation between  $r_I$  and the characteristic radii appearing in Table I. A blue solid curve shows  $r = r_I$ . Green solid and dashed curves are  $r = r_1^c$  and  $r = r_2^c$ , respectively. A gray dotted line denotes  $r = 3$ . Note that  $r_I > r_1^c$  holds for all the range of  $a$ , and  $r_I > r_2^c$  holds only for  $a < 0.6382\dots$ , and  $r_I > 3$  holds only for  $a < 0.7818\dots$ . Therefore, when we consider a



plunge orbit from the ISCO, all the cases in Table I appear only for  $a < 0.6382\dots$ ; on the other hand, only Cases (i)–(iii) appear for  $0.6382\dots \leq a < 0.7818\dots$ , and only Cases (i)–(ii) appear for  $0.7818\dots \leq a < 1$ . The Schwarzschild case  $a = 0$  is special because  $r_i^c = 3$  and will be discussed in Appendix A.

The equations of motion (7)–(9) for the emitter are reduced to

$$\dot{t} = \frac{E(1 + a^2 u^2) - 2a(L - aE)u^3}{a^2(u - u_+)(u - u_-)}, \quad (38)$$

$$\dot{\varphi} = \frac{Lu^2 - 2(L - aE)u^3}{a^2(u - u_+)(u - u_-)}, \quad (39)$$

$$\dot{u} = \sqrt{2}(L - aE)u^2(u - u_I)^{3/2}, \quad (40)$$

where  $\sigma_r = -1$ , and we have introduced a new variable  $u = r^{-1}$  and constants  $u_+ = r_H^{-1}$ ,  $u_- = r_-^{-1} = (1 - \sqrt{1 - a^2})^{-1}$ , and  $u_I = r_I^{-1}$ . Solving these equations, we obtain

$$\tau - \tau_0 = -\frac{\sqrt{2}}{(L - aE)u_I^2\sqrt{u - u_I}} {}_2F_1\left(-\frac{1}{2}, 2; \frac{1}{2}; 1 - \frac{u}{u_I}\right), \quad (41)$$

$$\begin{aligned} t - t_0 = \frac{1}{\sqrt{2}a^2(L - aE)} & \left[ -\frac{4[E - a(L - aE)u_I^2]}{u_I(u_+ - u_I)(u_- - u_I)\sqrt{u - u_I}} + \frac{a^2E(u_I - 3u)}{u_I^2u\sqrt{u - u_I}} \right. \\ & - \frac{a^2E(3 + 4u_I)}{u_I^{5/2}} \tan^{-1}\left(\sqrt{\frac{u - u_I}{u_I}}\right) \\ & + \frac{4(aLu_- - 2E)}{(u_- - u_+)(u_- - u_I)^{3/2}} \tanh^{-1}\left(\sqrt{\frac{u - u_I}{u_- - u_I}}\right) \\ & \left. - \frac{4(aLu_+ - 2E)}{(u_- - u_+)(u_+ - u_I)^{3/2}} \tanh^{-1}\left(\sqrt{\frac{u - u_I}{u_+ - u_I}}\right) \right], \quad (42) \end{aligned}$$

$$\begin{aligned} \varphi - \varphi_0 = \frac{\sqrt{2}}{a^2(L - aE)} & \left[ -\frac{L - 2(L - aE)u_I}{(u_+ - u_I)(u_- - u_I)\sqrt{u - u_I}} \right. \\ & + \frac{L - 2(L - aE)u_+}{(u_- - u_+)(u_+ - u_I)^{3/2}} \tanh^{-1}\left(\sqrt{\frac{u - u_I}{u_+ - u_I}}\right) \\ & \left. - \frac{L - 2(L - aE)u_-}{(u_- - u_+)(u_- - u_I)^{3/2}} \tanh^{-1}\left(\sqrt{\frac{u - u_I}{u_- - u_I}}\right) \right], \quad (43) \end{aligned}$$

where  $\tau$  is proper time, and  ${}_2F_1$  is the Gaussian hypergeometric function, and  $\tau_0$ ,  $t_0$ , and  $\varphi_0$  are arbitrary constants and are set to zero in the following. Further assume that the radial position of the emitter,  $r_*(\tau)$ , at initial time  $\tau = \tau_i$  is given by

$$r_*(\tau_i) = r_I - \epsilon, \quad (44)$$

where  $0 < \epsilon \ll 1$ .<sup>1</sup> It is worth noting that the plunge orbit does not depend on the choice of  $\epsilon$ ; in other words, it is unique up to the gauge freedom of  $\tau$ ,  $t$ , and  $\varphi$ . The initial radial velocity

<sup>1</sup> In the limit  $\epsilon \rightarrow 0$ , then  $\tau_i \rightarrow -\infty$ .

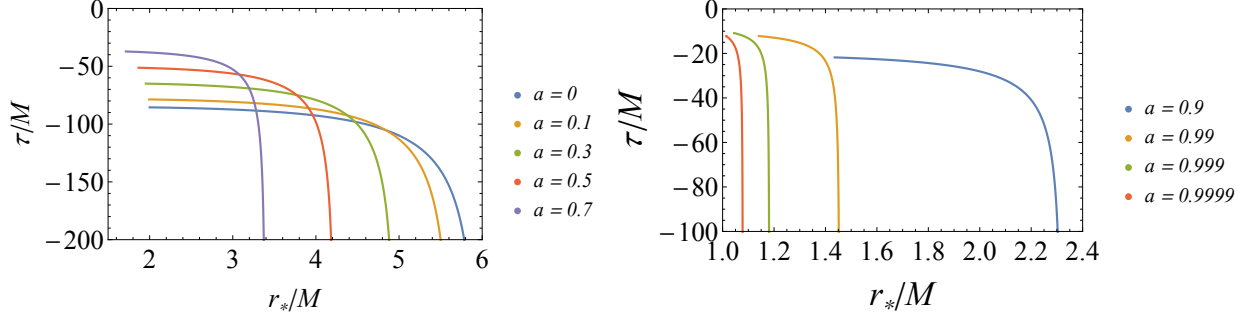


FIG. 3. Radial motion of the emitter for each value of  $a$ . It falls from the vicinity of the ISCO into the horizon. Each curve terminates at the horizon radius.

$\dot{r}_*(\tau_i)$  is determined through Eq. (40). The change of  $r_*(\tau)$  in Eq. (41) is shown in Fig. 3. Each curve gradually decreases as  $\tau$  increases, and it eventually terminates at the horizon,  $r_*(\tau_f) = r_H$ , which means that the time duration  $\tau_f - \tau_i$  is always finite. As seen in Eq. (42), however, the corresponding coordinate time duration is infinite because of the infinite gravitational redshift at the horizon. Typically, the emitter leaving from the vicinity of the ISCO will orbit with little change in its orbital radius for a while, i.e., the radial velocity component will be relatively small in an early phase. After that, the radial velocity will gradually increase and eventually shift into a plunging orbit toward the horizon. Figure 4 shows examples of the plunge orbits for  $a = 0$  and  $a = 0.9$ .

## V. PHOTON ESCAPE PROBABILITY

To evaluate the escape probability of a photon isotropically emitted from the emitter, we introduce a tetrad frame at rest with respect to the emitter,  $\zeta_*^{(\mu)} = \zeta^{(\mu)}|_{r=r_*, \theta=\theta_*}$ , where

$$\zeta^{(0)} = -E dt - \frac{\sqrt{R_1}}{\Delta} dr + L d\varphi, \quad (45)$$

$$\zeta^{(1)} = \frac{1}{\sqrt{\rho^2 - r^2 \Delta A}} \left[ -2a\sqrt{R_1} dt + Lr^3 dr + \frac{A}{r} \sqrt{R_1} d\varphi \right], \quad (46)$$

$$\zeta^{(2)} = r d\theta, \quad (47)$$

$$\zeta^{(3)} = \frac{1}{\sqrt{\rho^2 - r^2 \Delta A}} \left[ (r^2 \Delta - E\rho) dt - \frac{\rho\sqrt{R_1}}{\Delta} dr + L\rho d\varphi \right], \quad (48)$$

where  $\zeta_*^{(0)}$  coincides with the momentum of the emitter, and

$$\rho = EA - 2aLr. \quad (49)$$

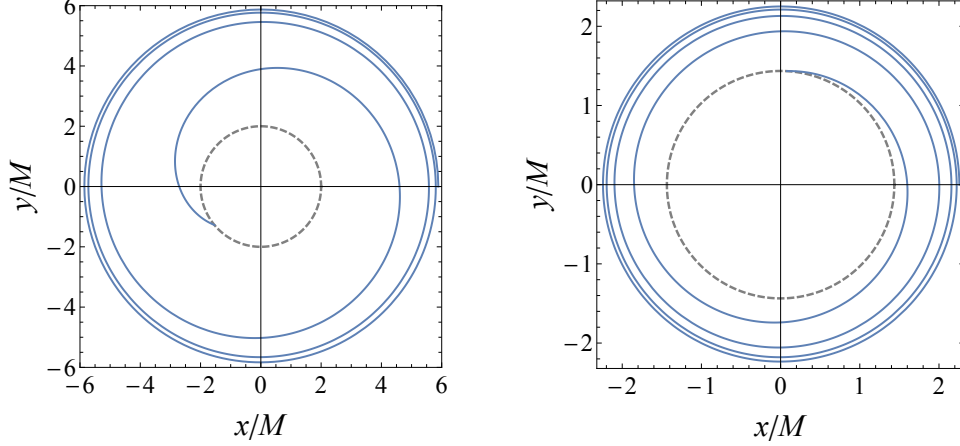


FIG. 4. Top view of the plunge trajectories of an emitter from the vicinity of the ISCO into the horizon. The blue solid curves show the plunge orbits, and the gray dashed circles denote the horizon radii. The left figure shows the case  $a = 0$ , for which  $r_H = 2$  and  $r_I = 6$ , and the initial condition is chosen as  $\epsilon = 0.1118$ . The right figure shows the case  $a = 0.9$ , for which  $r_H \simeq 1.4358$  and  $r_I \simeq 2.3208$ , and the initial condition is chosen as  $\epsilon = 0.06379$ . The size of each frame coincides with each ISCO radius. The coordinates are defined by  $(x, y) = (r \cos \psi, r \sin \psi)$ , where  $\psi$  is the angle in the ingoing Kerr-Schild coordinates (see Appendix B).

The tetrad components of the photon momentum in this frame are  $k_*^{(\mu)} = k^{(\mu)}|_{r=r_*, \theta=\theta_*}$ , where  $k^{(\mu)} = k^a \zeta_a^{(\mu)}$  are given by

$$k^{(0)} = \frac{br[2aE + L(r-2)] - \rho - \sigma_r \sqrt{R_0 R_1}}{r^2 \Delta}, \quad (50)$$

$$k^{(1)} = \frac{r(\sigma_r L \sqrt{R_0} + b \sqrt{R_1})}{\sqrt{\rho^2 - r^2 \Delta A}}, \quad (51)$$

$$k^{(2)} = \sigma_\theta \frac{\sqrt{q}}{r}, \quad (52)$$

$$k^{(3)} = \frac{Lr\rho[2a + b(r-2)] - (A - 2abr)(E\rho - r^2 \Delta) - \sigma_r \rho \sqrt{R_0 R_1}}{r^2 \Delta \sqrt{\rho^2 - r^2 \Delta A}}. \quad (53)$$

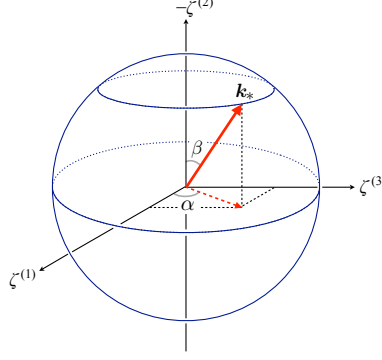
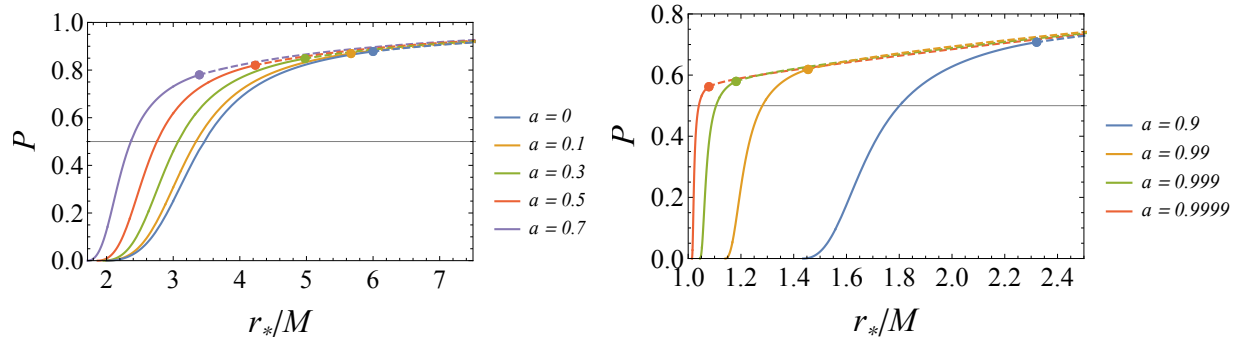
Note that  $\sigma_r$  and  $\sigma_\theta$  are for an emitted photon. We can relate the impact parameters  $(b, q)$  to the emission angle  $(\alpha, \beta)$  measured in the rest frame by

$$\cos \alpha = \frac{k_*^{(1)}}{\sqrt{(k_*^{(1)})^2 + (k_*^{(3)})^2}}, \quad \sin \alpha = \frac{k_*^{(3)}}{\sqrt{(k_*^{(1)})^2 + (k_*^{(3)})^2}}, \quad (54)$$

$$\cos \beta = \frac{k_*^{(2)}}{k_*^{(0)}}, \quad \sin \beta = -\frac{\sqrt{(k_*^{(1)})^2 + (k_*^{(3)})^2}}{k_*^{(0)}}, \quad (55)$$

where the sign of  $\cos \beta$  flips only with the sign flip of  $\sigma_\theta$ . Figure 5 illustrates the relation between  $k_*^{(\mu)}$  and  $(\alpha, \beta)$ . Then, we define the photon escape probability as

$$P(r_*; a) = \frac{1}{4\pi} \iint_{\mathcal{E}} d\alpha \wedge d\beta, \quad (56)$$

FIG. 5. Emission angles  $(\alpha, \beta)$  defined at the rest frame of the emitter.FIG. 6. Photon escape probability  $P(r_*; a)$  for each value of  $a$ . Solid curves: the escape probabilities of a photon emitted from the emitter plunging from the ISCO into the horizon. Dashed curves and dots are the escape probabilities of a photon emitted from an emitter on circular geodesics and the ISCO, respectively.

where  $\mathcal{E}$  denotes the whole parameter region of escape photons in the  $(\alpha, \beta)$  plane (i.e., the photon escape cone [12, 20, 24]). The region  $\mathcal{E}$  are translated from the photon escape parameter region in Table I. One of the practical ways to evaluate  $P$  is shown in Appendix C.

Figure 6 shows  $P$  of  $r_*$  for a fixed value of  $a$ , which are shown by solid curves. Each dashed curve shows the escape probability of a photon emitted from an emitter orbiting circular geodesics [3]. Each dot at the connection between solid and dashed curves shows the limit value  $P(r_I; a)$  in the limit  $r_* \rightarrow r_I$  (i.e.,  $\epsilon \rightarrow 0$ ).<sup>2</sup> We find that once the emitter gently starts to fall from the vicinity of the ISCO, the probability  $P$  decreases monotonically with  $r_*$ . Even when the emitter crosses the unstable photon circular orbit radii,  $P$  shows no characteristic behavior. As the left endpoint of each curve shows,  $P$  vanishes when the emitter reaches the horizon.

As the emitter moves along the plunge orbit,  $P$  will certainly be less than a half somewhere along the way (see gray lines in Fig. 6). Let  $r_0$  be the radius at which  $P = 1/2$ . For  $a = 0$ , we find

<sup>2</sup> The value  $P(r_I; a)$  decreases as  $a$  increases but approaches to a finite value  $P = 0.5464\dots$  even in the extremal limit  $a \rightarrow 1$  [3, 4].

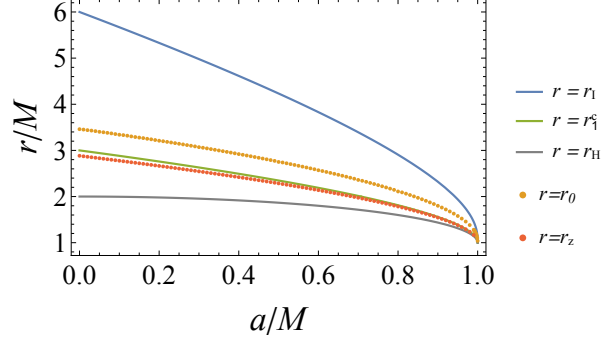


FIG. 7. Plots of  $r_0$  and  $r_z$ . Orange dots:  $r = r_0$ . Red dots:  $r = r_z$ . Blue solid curve: the ISCO radius given by Eq. (35). Green solid curve: the radius of photon circular prograde orbit given by Eq. (24). Gray solid curve: the horizon radius.

TABLE II. Numerical values of characteristic radii for several values of  $a$ .

$a$	0	0.1	0.2	0.3	0.4	0.5	0.6	0.7	0.8	0.9	0.99	0.999	0.9999
$r_I$	6	5.6693	5.3294	4.9786	4.6143	4.2330	3.8290	3.3931	2.9066	2.3208	1.4544	1.1817	1.0785
$r_0$	3.46	3.34	3.21	3.07	2.92	2.75	2.57	2.36	2.11	1.80	1.28	1.10	1.04
$r_1^c$	3	2.8821	2.7591	2.6300	2.4933	2.3472	2.1889	2.0133	1.8110	1.5578	1.1676	1.0520	1.0163
$r_z$	2.883	2.775	2.663	2.545	2.419	2.285	2.138	1.974	1.784	1.543	1.167	1.051	1.017
$r_H$	2	1.9949	1.9797	1.9539	1.9165	1.8660	1.8	1.7141	1.6	1.4358	1.1410	1.0447	1.0141

that  $r_0 \simeq 3.46$ , which is outside the photon sphere at  $r = 3$ . Since the photon escape probability for a static light source is just a half at  $r = 3$  [12], our result shows that  $P$  tends to be suppressed by the effect of the proper motion [see also Fig. 8(a)]. Several values of  $r_0$  are summarized in Table II, and the plots of  $r_0$  are shown in Fig. 7 (see orange dots). The radius  $r_0$  decreases monotonically as  $a$  increases. We can roughly evaluate  $r_0$  as being approximately intermediate value between  $r_I$  and  $r_H$ ,

$$\frac{2r_0}{r_I + r_H} \simeq 1. \quad (57)$$

Therefore, if we adopt  $r_0$  as one of the indicators that divides the region where plunge orbits are observable or not, we can conclude that our plunge orbits are observable up to the middle of  $r_I$  and  $r_H$ .

Similarly for the case  $a \neq 0$ , it is useful to compare  $r_0$  with the radius at which the escape probability of a photon emitted from an emitter stationary relative to the black hole [i.e., an emitter at rest in the locally nonrotating frame (LNRF)] is a half, where the LNRF is given by

$$e^{(0)} = \sqrt{\frac{\Sigma\Delta}{A}}dt, \quad e^{(1)} = \sqrt{\frac{\Sigma}{\Delta}}dr, \quad e^{(2)} = \sqrt{\Sigma}d\theta, \quad e^{(3)} = \sqrt{\frac{A}{\Sigma}}\sin\theta\left(d\varphi - \frac{2ar}{A}dt\right). \quad (58)$$

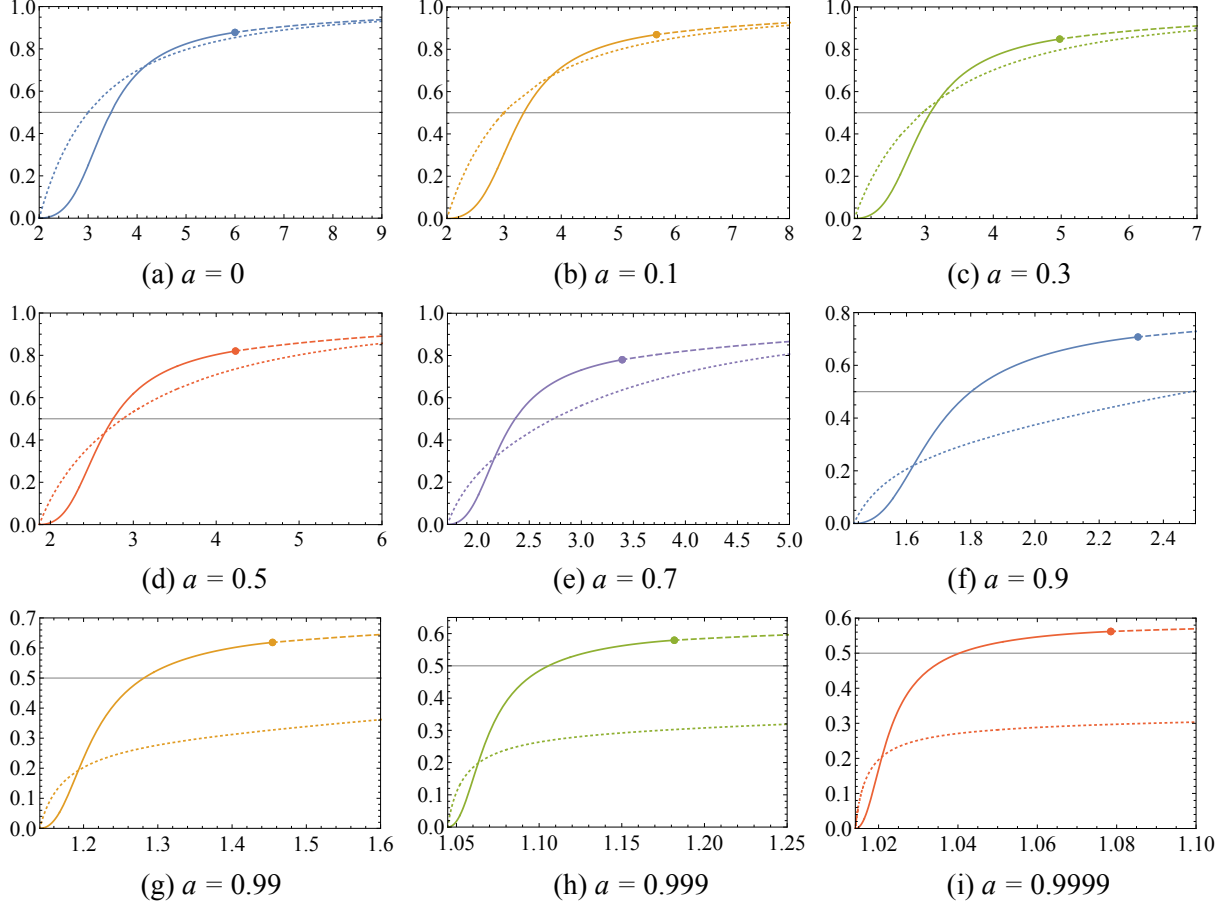


FIG. 8. Escape probabilities of a photon emitted from an emitter in various states of motion. Solid curves denote  $P$ , and dotted curves denote  $P_L$ , as functions of  $r_*$ . Dashed curves: the escape probabilities of a photon emitted from an emitter on circular geodesics.

Recall that the LNRF reduces to the static frame in the Schwarzschild case ( $a = 0$ ). Figure 8 shows the comparisons between  $P$  in Eq. (56) (solid curves) and the escape probability of a photon emitted from a rest source at the LNRF,  $P_L$  (dotted curves). We can regard  $P_L$  as the photon escape probability that is not affected by the proper motion of an emitter. With  $P_L$  as the reference, for all  $a$ , we find that  $P > P_L$  in the early phase. We can interpret it as an increase in  $P$  due to the effect of the proper  $\varphi$ -motion, i.e., the relativistic beaming toward spatial infinity occurs. On the other hand, we find that  $P < P_L$  in the late phase. We can interpret it as the suppression of  $P$  due to the increase of the velocity ratio

$$\nu = |v_*^{(1)}/v_*^{(3)}| \quad (59)$$

in the late phase, where  $v_*^{(i)}$  are the 3-velocity components relative to the LNRF,

$$v_*^{(i)} = \left. \frac{u^a e_a^{(i)}}{u^a e_a^{(0)}} \right|_{r=r_*, \theta=\theta_*}. \quad (60)$$

The ratio  $\nu$  monotonically increases from nearly zero at the initial point to infinity at the horizon. In other words, as the effect of the proper  $r$ -motion increases, the rate of the relativistic beaming toward the black hole increases, and as a result,  $P$  is suppressed. Let  $r_{0,L}$  be the radius at which  $P_L = 1/2$ . For  $a \lesssim 0.401$ , we have  $r_0 > r_{0,L}$ . This means that the proper motion of the emitter acts to suppress  $P$  and makes a negative contribution to observability. However, for  $a \gtrsim 0.401$ , we have  $r_0 < r_{0,L}$ . In other words, the proper motion of the emitter acts to increase  $P$  and expands the observable region toward the horizon.

Let us focus on the frequency shift of escape photons. Let  $z$  be the blueshift factor distribution of photons emitted from the emitter,

$$z = 1 + k_*^{(0)}. \quad (61)$$

Figure 9 shows the maximum value  $z_{\max}$  of the blueshift factor  $z$ , where the corresponding parameters are  $(b, q, \sigma_r) = (b_1(r_*; 0), 0, 1)$  for  $r_* \geq r_1^c$  (solid curves) and  $(b, q, \sigma_r) = (b_1^c, 0, 1)$  for  $r_H < r_* < r_1^c$  (dash-dotted curves). Dashed curves and dots in the range  $r_* \geq r_1$  also denote the maximum blueshift factor of an escape photon emitted from an emitter orbiting circular geodesics and the ISCO, respectively, where the corresponding parameters are  $(b, q, \sigma_r) = (b_1(r_*; 0), 0, 1)$ . Let  $r_z$  be the radius at which  $z_{\max} = 0$ . For all  $a$ , we have  $z_{\max} > 0$  in the range  $r > r_z$ , i.e., the energy of escape photons can blueshift there. On the other hand, we have  $z_{\max} < 0$  in the range  $r < r_z$ . This means that all the escape photons are no longer blueshifted in this region. Several values of  $r_z$  are shown in Table II and are plotted in Fig. 7. We see that  $r_0 > r_z$  for all  $a$ . This implies that the Doppler blueshift due to the emitter proper motion is dominant and can sufficiently cancel the gravitational redshift in the observation of the emitter in the range  $r > r_0$ .

## VI. SUMMARY AND DISCUSSIONS

We have considered isotropic photon emission from an emitter moving near the Kerr black hole. Clarifying necessary and sufficient escape conditions for photons emitted from the equatorial plane, we have specified whole parameter regions of photon escape in the two-dimensional impact parameter space without restricting the radial position of the emission. We have focused on the dynamics of an emitter, which falls gently from the ISCO and plunges into the black hole horizon.

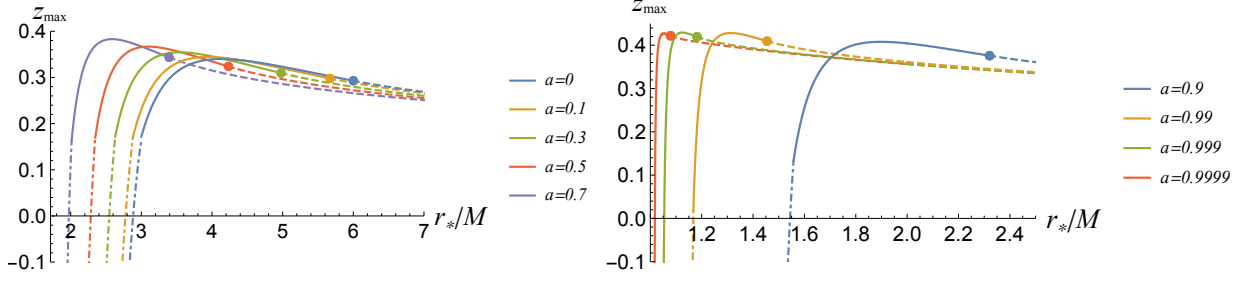


FIG. 9. Maximum blueshift. Solid curves:  $z_{\max}$  in the range  $r_1^c \leq r_* < r_I$ . Dash-dotted curves:  $z_{\max}$  in the range  $r_H < r_* < r_1^c$ . Dashed curves and dots: the maximum blueshift of an escape photon emitted from an emitter orbiting circular geodesics and the ISCO, respectively.

Assuming initial conditions of the emitter to be adiabatically shifted slightly inward from the ISCO radius, we have obtained the unique plunge orbits analytically. In the early phase, the emitter orbits the black hole many times in the vicinity of the ISCO, and eventually, it turns to plunge toward the horizon in the late phase.

We have defined the escape probability  $P$  of a photon isotropically emitted from the emitter and have shown that  $P$  decreases monotonically with the radial position of the emitter. In this paper, we have supposed that the emitter is observable if  $P > 1/2$ . For any black hole spin parameter,  $P$  is greater than  $1/2$  initially. As it falls toward the center and passes through  $r = r_0$ , the probability eventually becomes less than a half. Therefore, we have concluded that the emitter is observable until it reaches  $r = r_0$ , which is estimated as approximately intermediate value between the radii of the ISCO and the horizon. We have further clarified that  $P$  depends on the proper motion of the emitter. The probability is larger than the reference value  $P_L$  due to proper  $\varphi$ -motion in the early phase, while in the late phase,  $P$  is smaller than  $P_L$  due to proper  $r$ -motion. However, for  $a \lesssim 0.401$ , the proper motion acts to make  $r_0$  larger; in other words, it makes a negative contribution to observability. On the other hand, for  $a \gtrsim 0.401$ , the proper motion acts to make  $r_0$  smaller, which means that the proper motion positively affects the observability, and we can continue to observe the emitter closer to the horizon. Furthermore, we have seen that the Doppler shift due to the proper motion can cancel the gravitational redshift and can cause blueshift.

The distribution of the blueshift factor may contain additional characteristics related to the proper motion, which will be reported in a separate paper in detail.<sup>3</sup> The quantities we have discussed here, the escape cone  $\mathcal{E}$ , the photon escape probability  $P$ , and the blueshift factor distribution  $z$ , provide a basis for evaluating observables such as energy fluxes. The evaluation and

<sup>3</sup> It was recently discussed that the maximum blueshift of a light source falling vertically in the radial direction in the Schwarzschild black hole spacetime is related to the light ring [25].



TABLE III. Photon escape parameter region in the Schwarzschild spacetime ( $a = 0$ ).

Case	$\sigma_r = +$	$\sigma_r = -$
$2 < r_* < 3$	$q + b^2 < 27$	n/a
$r_* \geq 3$	$q + b^2 \leq q_{\max}$	$27 < q + b^2 < q_{\max}$

characterization of such physical quantities are left for future work.

We have assumed a small value for the radial initial velocity of our emitter, which is justified in the standard disk model. In the radiatively inefficient accretion flow model, we may have to assume a larger value for its initial velocity. This is also left for future work.

## ACKNOWLEDGMENTS

The authors are grateful to Takahiko Matsubara, Toyokazu Sekiguchi, Takahiro Tanaka, Norichika Sago, Keisuke Nakashi, Chul-Moon Yoo, Kouji Nakamura, Takaaki Ishii, Hiroyuki Nakano, and Hirotaka Yoshino for useful comments. This work was supported by JSPS KAKENHI Grants No. JP19K14715 (T.I.), No. JP20K14467, No. JP20J00416 (K.O.), No. JP17H01131, No. JP19H05114, and No. JP20H04750 (K.K.).

## Appendix A: SCHWARZSCHILD CASE ( $a = 0$ )

### 1. PHOTON ESCAPE CONDITIONS

In the Schwarzschild case  $a = 0$ , the radial equation of motion (9) reduces to

$$\dot{r}^2 + V(r) = \frac{1}{q + b^2}, \quad (\text{A1})$$

$$V(r) = \frac{1}{r^2} - \frac{2}{r^3}, \quad (\text{A2})$$

where we have rescaled  $\tau$  by  $(q + b^2)^{1/2}$ . The function  $V$  is the familiar effective potential of photon motion and is related to  $b_i$  in Eqs. (17) and (18) as  $V = (q + b_i^2)^{-1}$ . It takes a local maximum value  $V = 1/27$  at  $r = 3$  (i.e.,  $r_i^c = 3$ ). As a result, the photon escapable parameter region in Table I reduces to Table III, where we have used  $q + (b_i^s)^2 = 27$  and  $q_{\max} = V^{-1}(r_*)$ .

## 2. Dynamics of an emitter

We consider the plunge orbit of Sec. IV in the case of the Schwarzschild spacetime. The energy and angular momentum of the emitter reduces to  $E = 2\sqrt{2}/3$  and  $L = 2\sqrt{3}$ , respectively. Then, Eqs. (38)–(40) reduce to

$$\dot{t} = \frac{Er}{r-2}, \quad (\text{A3})$$

$$\dot{\varphi} = \frac{L}{r^2}, \quad (\text{A4})$$

$$\dot{r} = -\frac{1}{3} \left( \frac{6}{r} - 1 \right)^{3/2}, \quad (\text{A5})$$

where we have used  $r_H = 2$  and  $r_I = 6$ . Integrating these equations, we obtain

$$\frac{r_I}{r} = 1 + \frac{L^2}{(\varphi - \varphi_0)^2}, \quad (\text{A6})$$

$$t - t_0 = -\frac{2\sqrt{2}(24u-1)}{u\sqrt{6u-1}} - 44\sqrt{2} \tan^{-1}(\sqrt{6u-1}) + 4 \tanh^{-1}(\sqrt{(6u-1)/2}), \quad (\text{A7})$$

which correspond to Eqs. (42) and (43) for  $a = 0$ , respectively. These results coincide with those of Ref. [23].

## Appendix B: INGOING KERR-SCHILD COORDINATES

The dynamics of particles near the horizon is not well described in the Boyer-Lindquist coordinates because  $(dt)_a$  and  $(d\varphi)_a$  are singular in the horizon limit (i.e., the norms  $\|dt\|, \|d\varphi\| \rightarrow \infty$  as  $r \rightarrow r_H$ ). As seen in Eqs. (7) and (8) or Eqs. (38) and (39), even though  $u^a$  is regular on the horizon, the components  $\dot{t} = u^a(dt)_a$  and  $\dot{\varphi} = u^a(d\varphi)_a$  diverge in the horizon limit. Therefore, it is useful to adopt the ingoing Kerr-Schild coordinates  $(v, r, \theta, \psi)$ , which are regular even on the future horizon, rather than the Boyer-Lindquist coordinates to describe the dynamics of particles near the horizon. The coordinate transformation between these coordinates (see, e.g., Ref. [26]) are given by

$$v = t + \int \frac{r^2 + a^2}{\Delta} dr = t + r + \frac{Mr_H}{\sqrt{M^2 - a^2}} \ln \left| \frac{r}{r_H} - 1 \right| - \frac{Mr_-}{\sqrt{M^2 - a^2}} \ln \left| \frac{r}{r_-} - 1 \right|, \quad (\text{B1})$$

$$\psi = \varphi + \int \frac{a}{\Delta} dr = \varphi + \frac{a}{2\sqrt{M^2 - a^2}} \ln \left| \frac{r - r_H}{r - r_-} \right|. \quad (\text{B2})$$

Then, the metric in the ingoing Kerr-Schild coordinates is given by

$$ds^2 = - \left( 1 - \frac{2Mr}{\Sigma} \right) dv^2 + 2dvdr + \Sigma d\theta^2 + \frac{A}{\Sigma} \sin^2 \theta d\psi^2 - 2a \sin^2 \theta dr d\psi - \frac{4Mar}{\Sigma} \sin^2 \theta dv d\psi. \quad (\text{B3})$$

### Appendix C: EVALUATION OF THE PHOTON ESCAPE PROBABILITY

We demonstrate one of the practical ways to evaluate  $P$  in Eq. (56). Let  $(\alpha_{\text{crit}}, \beta_{\text{crit}})$  be the values of  $(\alpha, \beta)$  evaluated with  $\sigma_\theta = -1$ ,  $b = b_{\text{SPO}}(\xi)$ , and  $q = q_{\text{SPO}}(\xi)$ , which are the so-called critical angles of photon escape [20]. We define a function  $f_{\sigma_r}(r_*, \xi)$  in terms of these angles by

$$f_{\sigma_r}(r_*, \xi) = \frac{1}{2\pi} \cos \beta_{\text{crit}} \frac{d\alpha_{\text{crit}}}{d\xi} = \frac{1}{2\pi} \frac{\cos \beta_{\text{crit}}}{\cos \alpha_{\text{crit}}} \frac{d \sin \alpha_{\text{crit}}}{d\xi}. \quad (\text{C1})$$

Then, the photon escape probability  $P$  is written as

$$P(r_*; a) = p + \Theta(-p), \quad (\text{C2})$$

where  $\Theta$  is a step function (i.e.,  $\Theta(\eta) = 1$  for  $\eta \geq 0$  and  $\Theta(\eta) = 0$  for  $\eta < 0$ ), and

$$p(r_*; a) = \begin{cases} \int_{r_2^c}^{r_1^c} f_1 d\xi & (r_H < r_* < r_1^c), \\ \int_{r_2^c}^{r_*} f_1 d\xi + \int_{r_*}^{r_1^c} f_{-1} d\xi & (r_1^c \leq r_* < r_2^c), \\ \int_{r_2^c}^{r_1^c} f_{-1} d\xi & (r_* > r_2^c). \end{cases} \quad (\text{C3})$$

$$p(r_*; a) = \begin{cases} \int_{r_2^c}^{r_*} f_1 d\xi + \int_{r_*}^{r_1^c} f_{-1} d\xi & (r_1^c \leq r_* < r_2^c), \\ \int_{r_2^c}^{r_1^c} f_{-1} d\xi & (r_* > r_2^c). \end{cases} \quad (\text{C4})$$

$$p(r_*; a) = \begin{cases} \int_{r_2^c}^{r_1^c} f_{-1} d\xi & (r_* > r_2^c). \end{cases} \quad (\text{C5})$$

- [1] K. Akiyama *et al.* (Event Horizon Telescope Collaboration), First M87 Event Horizon Telescope results. I. The shadow of the supermassive black hole, *Astrophys. J.* **875**, L1 (2019) [arXiv:1906.11238 [astro-ph.GA]].
- [2] T. Igata, H. Ishihara, and Y. Yasunishi, Observability of spherical photon orbits in near-extremal Kerr black holes, *Phys. Rev. D* **100**, 044058 (2019) [arXiv:1904.00271 [gr-qc]].
- [3] T. Igata, K. Nakashi, and K. Ogasawara, Observability of the innermost stable circular orbit in a near-extremal Kerr black hole, *Phys. Rev. D* **101**, 044044 (2020) [arXiv:1910.12682 [astro-ph.HE]].
- [4] D. E. A. Gates, S. Hadar, and A. Lupsasca, Photon emission from circular equatorial Kerr orbiters, *Phys. Rev. D* **103**, 044050 (2021) [arXiv:2010.07330 [gr-qc]].
- [5] C. T. Cunningham and J. M. Bardeen, The optical appearance of a star orbiting an extreme Kerr black hole, *Astrophys. J.* **183**, 237 (1973).
- [6] D. E. A. Gates, S. Hadar, and A. Lupsasca, Maximum observable blueshift from circular equatorial Kerr orbiters, *Phys. Rev. D* **102**, 104041 (2020) [arXiv:2009.03310 [gr-qc]].
- [7] R. Abuter *et al.* (GRAVITY Collaboration), Detection of the gravitational redshift in the orbit of the star S2 near the Galactic centre massive black hole, *Astron. Astrophys.* **615**, L15 (2018) [arXiv:1807.09409 [astro-ph.GA]].
- [8] H. Saida, S. Nishiyama, T. Ohgami, Y. Takamori, M. Takahashi, Y. Minowa, F. Najarro, S. Hamano, M. Omiya, and A. Iwamatsu, A significant feature in the general relativistic time evolution of the

- redshift of photons coming from a star orbiting Sgr A\*, *Publ. Astron. Soc. Jpn.* **71**, 126 (2019) [arXiv:1910.02632 [gr-qc]].
- [9] Y. Takamori, S. Nishiyama, T. Ohgami, H. Saida, R. Saitou, and M. Takahashi, Constraints on the dark mass distribution surrounding Sgr A\*: Simple  $\chi^2$  analysis for the redshift of photons from orbiting stars, arXiv:2006.06219 [astro-ph.GA].
  - [10] R. Abuter *et al.* (GRAVITY Collaboration), Detection of orbital motions near the last stable circular orbit of the massive black hole SgrA\*, *Astron. Astrophys.* **618**, L10 (2018) [arXiv:1810.12641 [astro-ph.GA]].
  - [11] Y. Iwata, T. Oka, M. Tsuboi, M. Miyoshi, and S. Takekawa, Time variations in the flux density of Sgr A\* at 230 GHz detected with ALMA, *Astrophys. J. Lett.* **892**, L30 (2020) [arXiv:2003.08601 [astro-ph.HE]].
  - [12] J. L. Synge, The escape of photons from gravitationally intense stars, *Mon. Not. R. Astron. Soc.* **131**, 463 (1966).
  - [13] T. Shiromizu, Y. Tomikawa, K. Izumi, and H. Yoshino, Area bound for a surface in a strong gravity region, *Prog. Theor. Exp. Phys.* **2017**, 033E01 (2017) [arXiv:1701.00564 [gr-qc]].
  - [14] C.-M. Claudel, K. S. Virbhadra, and G. F. R. Ellis, The geometry of photon surfaces, *J. Math. Phys. (N.Y.)* **42**, 818 (2001) [arXiv:gr-qc/0005050].
  - [15] D. V. Gal'tsov and K. V. Kobialko, Completing characterization of photon orbits in Kerr and Kerr-Newman metrics, *Phys. Rev. D* **99**, 084043 (2019) [arXiv:1901.02785 [gr-qc]].
  - [16] Y. Koga, T. Igata, and K. Nakashi, Photon surfaces in less symmetric spacetimes, *Phys. Rev. D* **103**, 044003 (2021) [arXiv:2011.10234 [gr-qc]].
  - [17] M. Walker and R. Penrose, On quadratic first integrals of the geodesic equations for type {22} spacetimes, *Commun. Math. Phys.* **18**, 265 (1970).
  - [18] B. Carter, Global structure of the Kerr family of gravitational fields, *Phys. Rev.* **174**, 1559 (1968).
  - [19] E. Teo, Spherical photon orbits around a Kerr black hole, *Gen. Relativ. Gravit.* **35**, 1909 (2003).
  - [20] K. Ogasawara, T. Igata, T. Harada, and U. Miyamoto, Escape probability of a photon emitted near the black hole horizon, *Phys. Rev. D* **101**, 044023 (2020) [arXiv:1910.01528 [gr-qc]].
  - [21] K. Ogasawara and T. Igata, Complete classification of photon escape in the Kerr black hole spacetime, *Phys. Rev. D* **103**, 044029 (2021) [arXiv:2011.04380 [gr-qc]].
  - [22] J. M. Bardeen, W. H. Press, and S. A. Teukolsky, Rotating black holes: Locally nonrotating frames, energy extraction, and scalar synchrotron radiation, *Astrophys. J.* **178**, 347 (1972).
  - [23] S. Hadar and B. Kol, Post-ISCO ringdown amplitudes in extreme mass ratio inspiral, *Phys. Rev. D* **84**, 044019 (2011) [arXiv:0911.3899 [gr-qc]].
  - [24] O. Semerák, Photon escape cones in the Kerr field, *Helv. Phys. Acta* **69**, 69 (1996).
  - [25] V. Cardoso, F. Duque, and A. Foschi, The light ring and the appearance of matter accreted by black holes, arXiv:2102.07784 [gr-qc].

- [26] E. Poisson, *A Relativist's Toolkit: The Mathematics of Black-Hole Mechanics* (Cambridge University Press, Cambridge, England, 2004).